

Entry Atmospheric Flight Control Authority Impacts on GN&C and Trajectory Performance for Orion Exploration Flight Test 1

Luke W. McNamara *

NASA Johnson Space Center, Houston, Texas, 77058, USA

One of the key design objectives of NASA's Orion Exploration Flight Test 1 (EFT-1) is to execute a guided entry trajectory demonstrating GN&C capability. The focus of this paper is the flight control authority of the vehicle throughout the atmospheric entry flight to the target landing site and its impacts on GN&C, parachute deployment, and integrated performance. The vehicle's attitude control authority is obtained from thrusting 12 Reaction Control System (RCS) engines, with four engines to control yaw, four engines to control pitch, and four engines to control roll. The static and dynamic stability derivatives of the vehicle are determined to assess the inherent aerodynamic stability. The aerodynamic moments at various locations in the entry trajectory are calculated and compared to the available torque provided by the RCS system. Interaction between the vehicle's RCS engine plumes and the aerodynamic conditions are considered to assess thruster effectiveness. This document presents an assessment of Orion's flight control authority and its effectiveness in controlling the vehicle during critical events in the atmospheric entry trajectory.

Nomenclature

α	Angle of attack, deg
α_{total}	Total angle of attack, deg
β	Angle of sideslip, deg
γ	Flight-path angle, deg
θ	Angle of pitch, deg
θ'	Boundary layer momentum thickness
μ	Fluid Viscosity
μ	Statistical mean value of Monte Carlo
σ	Statistical standard deviation of Monte Carlo
Φ	Angle of bank, deg
ϕ	Angle of roll, deg
ψ	Angle of yaw, deg
CG	Center-of-Gravity
C_m	Coefficient of pitching moment about CG
C_n	Coefficient of yawing moment about CG
$C_{\mathcal{L}}$	Coefficient of rolling moment about CG
C_{m_q}	Dynamic derivative on pitch damping due to pitch rate
C_{n_r}	Dynamic derivative on yaw damping due to yaw rate
$C_{\mathcal{L}_p}$	Dynamic derivative on roll damping due to roll rate
C_{m_α}	Partial derivative of C_m about CG with respect to angle of attack, [1/deg]
C_{n_β}	Partial derivative of C_n about CG with respect to angle of sideslip, [1/deg]
$C_{\mathcal{L}_\beta}$	Partial derivative of $C_{\mathcal{L}}$ about CG with respect to angle of sideslip, [1/deg]

*Aerospace Engineer, Flight Mechanics & Trajectory Design Branch, luke.w.mcnamara@nasa.gov

F	Thrust force of jet
L/D	Lift-over-Drag Ratio, nd
L_{ref}	Reference Length
$Re_{\theta'}$	Reynolds number nondimensionalized with θ' reference length
r	Yaw Rate
r_{jet}	Position vector from CG to jet
S_{ref}	Reference surface area
T	Torque
q	Pitch Rate
q_{∞}	Free-stream dynamic pressure
u_e	Boundary layer edge velocity in x-direction
v_{∞}	Free-stream velocity
<i>ANTARES</i>	Advanced NASA Technology Architecture for Exploration Studies
<i>API</i>	Application Programming Interface
<i>CA</i>	Control Authority
<i>CFD</i>	Computational Fluid Dynamics
<i>CSU</i>	Configuration Software Unit
<i>DOF</i>	Degree-of-Freedom
<i>EFT – 1</i>	Exploration Flight Test 1
<i>EI</i>	Entry Interface
<i>EDL</i>	Entry, Descent & Landing
<i>FBC</i>	Forward Bay Cover
<i>GN&C</i>	Guidance Navigation and Control
<i>Max</i>	Statistical maximum value of Monte Carlo
<i>Min</i>	Statistical minimum value of Monte Carlo
<i>MPCV</i>	Multi-Purpose Crew Vehicle
<i>MRC</i>	Moment Reference Center
<i>PredGuid</i>	Predictive Guidance CSU
<i>RCS</i>	Reaction Control System
<i>RAMSES</i>	Rapid Algorithm MATLAB/Simulink® Engineering Simulation
<i>UF</i>	Uncertainty Factor

I. Introduction

In November of 2011 NASA approved the Orion Exploration Flight Test 1 (EFT-1) and scheduled it to be launched from Kennedy Space Flight Center in late 2013 or 2014 . This test flight will support the design of the Orion spacecraft that NASA is developing to launch astronauts to asteroids, the moon, Mars, and other destinations with NASA’s new heavy launch vehicle the Space Launch System (SLS). For the flight test, the Orion capsule will be carried to orbit by a United Launch Alliance (ULA) Delta IV Heavy. For EFT-1 Orion will orbit the Earth twice reaching a high-apogee orbit and then re-enter the atmosphere at near lunar return velocity. After re-entering the atmosphere, the vehicle will fly a guided entry profile via GN&C bank angle modulation. The trajectory will conclude with vehicle splashdown in the Pacific Ocean near San Diego, CA.

The GN&C software performs several key functions during the atmospheric entry. The guidance algorithm targets the landing site by modulating the vehicle’s bank angle in order to point its lift vector and steer the vehicle to the target location. The guidance system uses a Numeric Predictor Corrector (NPC) algorithm to target the bank angle at each guidance cycle to reduce the range-to-target errors in the longitudinal and lateral channels. Later the guidance algorithm switches to using a flight-tested legacy guidance software algorithm developed for the NASA Apollo missions in the 1960’s called Apollo Final Phase from the Apollo entry guidance algorithm.

The entry flight control system is activated 30 minutes prior to the Entry Interface (EI) altitude of 400,000 ft. During the exo-atmospheric portion of flight the control system maneuvers the vehicle to a heat-shield forward attitude and then maintains that orientation for aerocapture. During the atmospheric portion of flight, the control system works to actively target the bank angles commanded by guidance, and to null

disturbance body rates in the roll, pitch and yaw channels.

The driving objectives of the OFT1 entry trajectory are:

1. Maximum Bank Saturation for Entry Guidance Demonstration

It is desired that the maximum bank saturation during the final phase of the entry guidance remain below 50%. In order to accomplish this the Entry Interface state must be within the entry flight corridor of the vehicle. This objective ensures that all aspects of the entry guidance algorithm will be exercised, including both downrange and crossrange control.

2. Landing Accuracy

The landing accuracy requirement is for the vehicle to land within 10.8 nautical miles (n.mi.) of the desired landing site with a probability of 99.73% at 90% confidence. This probability equates to allowing 4 misses for a 3000 case Monte Carlo analysis.

3. Aerothermal Criteria

To meet the aerothermal test objective, it is desired that the flow over most of the heat shield be turbulent while the CM travels through peak heating. Reynolds number $Re_{\theta'}$ is a nondimensional parameter that measures the turbulence of a flow and is defined in Equation 1 using the boundary layer momentum thickness, θ' .

$$Re_{\theta'} = \frac{\rho_e u_e}{\mu_e} \theta' \quad (1)$$

It is desired that the value of $Re_{\theta'}$ on the Leeside Dish of the capsule reach a value of at least 250 before the freestream velocity decreases past 20,000 $\frac{ft}{sec}$. This is in order to ensure a transition to turbulent flow during the maximum heat pulse of the entry.

4. Determine CM RCS exoatmospheric and atmospheric performance.

The EFT-1 flight test will provide engineering data to the CM Propulsion team to demonstrate the operational performance of the CM RCS thrusters. The data will refine the predictions of the thruster performance based on pulse durations, engine temperature, atmospheric back pressure, scarfing effects, impacts of firing simultaneous jets, etc.

5. Determine RCS jet impingement aerothermodynamic environment during entry.

The EFT-1 flight test will provide engineering data to quantify the level of thruster jet interaction with the aerodynamic flow around the MPCV body. The concern is that the interaction could change the thrust direction and magnitude of the CM RCS thrusters and affect flight control authority and control stability.

6. CM RCS Thruster Pulse Cycle Capability

The EFT-1 flight test is designed operate under the CM RCS pulse cycle constraint specified by the propulsion system.

A. Background

The static and dynamic stability of the Orion vehicle result from the vehicle's aerodynamic moments and control authority. The aerodynamic moments of the vehicle vary during hypersonic, supersonic and subsonic flight. Similarly, the effective thrust vector direction and magnitude for each RCS thruster depends on the external atmospheric back pressure on each nozzle. If the aerodynamic RCS jet interaction effects are neglected the RCS jets' thrust magnitudes are indirectly a function of altitude via external atmospheric pressure. In that case, as altitude increases the thrust delivered by the jets increases until at a high altitude the curve plateaus at the vacuum thrust level. In reality though the external atmospheric back pressures are altered due to RCS plume jet interactions and hence this interaction's effects need to be considered.

1. EFT-1 Overview

The overview of EFT-1 trajectory and groundtrack is provided in Figure 1 below.

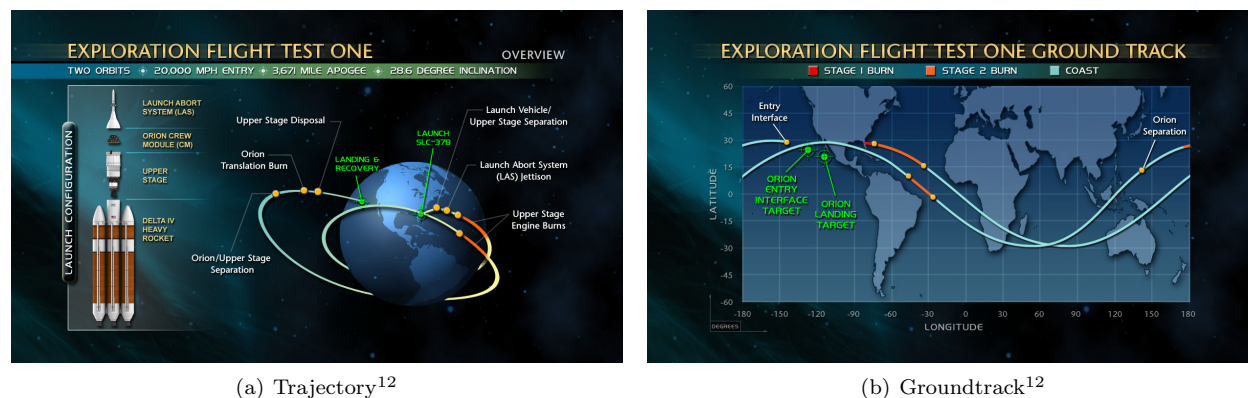


Figure 1. Overview

The relevant portion of the EFT-1 EDL flight, where the vehicle has active control authority, is illustrated in Figure 2 below.

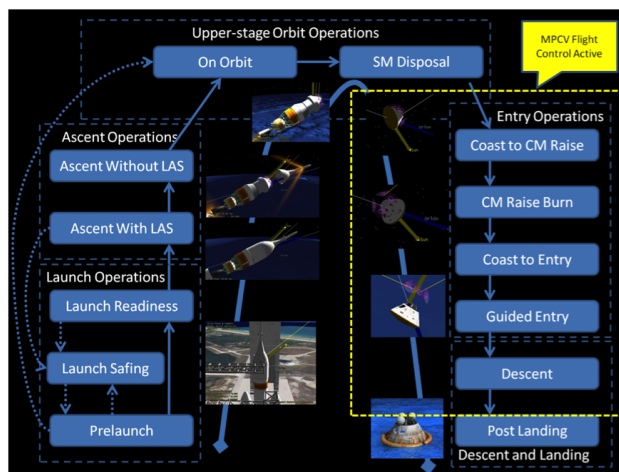


Figure 2. Orion Mission Phases: Indication of Active Flight Control Segments⁸

2. GNC Body Frame

The integrated performance results in this document are expressed in the GN&C Body Frame. This frame is illustrated in Figure 3 below.

B. Trajectory Design

The trajectories were produced with Advanced NASA Technology Architecture for Exploration Studies (ANTARES), a six Degree-of-Freedom (DOF) simulation, that numerically propagates the state vectors of the simulation bodies forward in time. ANTARES was configured to use Rapid Algorithm MATLAB/Simulink[®] Engineering Simulation (RAMSES) flight software. RAMSES is an auto-coded application from the original

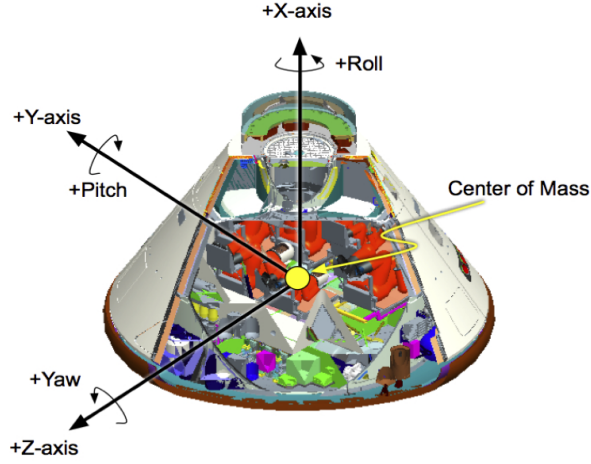


Figure 3. GNC Body Frame¹⁰

MATLAB/Simulink/Stateflow flight software artifacts representing the entire GN&C implementation for EFT-1. The PredGuid guidance algorithm which was employed uses a numerical predictor-corrector coupled with the Apollo Final Phase Entry Guidance. The Apollo Final Phase Entry Guidance and PredGuid algorithm have been well documented^{6,7}. Typically for EFT-1 Monte Carlo analysis is used to provide sensitivities to system and subsystem level performance impacts. These Monte Carlos include dispersions on the initial state vectors, aerodynamic uncertainties, atmospheric characteristics, navigation characteristics, propulsion characteristics, mass properties and more. These dispersions are drawn either from uniform or Gaussian distributions depending on the model. As a result of the use of the uniform distributions, the results are not purely Gaussian.

C. Aerodynamic Characteristics

The MPCV aerodynamic database is composed of CFD modeling anchored by wind tunnel testing. The database is produced by the MPCV Aerosciences Team. Currently the MPCV aerodynamic database version 0.60 is the approved version for modeling the Orion vehicle aerodynamics in the ANTARES trajectory simulation. As the entry trajectory is highly sensitive to changes in the aerodynamic model used, each database update necessitates reassessment of the integrated entry performance against objectives, requirements and performance metrics.

In the database the uncertainty ranges are specified for all of the aerodynamic coefficients. When ANTARES trajectories are propagated in dispersed Monte Carlo sets, the aerodynamic uncertainty values are drawn from uniform distributions constructed over the uncertainty ranges. For example, the aerodynamic moments C_l , C_m , and C_n and dynamic damping terms C_{l_p} , C_{m_q} , and C_{n_r} are modeled in this manner in Monte Carlo analysis.

The standard aerodynamic moment coefficients are given below in Equation 2.

$$\begin{aligned} C_m &= \frac{M}{q_\infty \cdot S_{ref} \cdot l_{ref}} \\ C_n &= \frac{N}{q_\infty \cdot S_{ref} \cdot l_{ref}} \\ C_{\mathcal{L}} &= \frac{\mathcal{L}}{q_\infty \cdot S_{ref} \cdot l_{ref}} \end{aligned} \quad (2)$$

where

$$q_\infty = \frac{1}{2} \rho_\infty v_\infty^2 \quad (3)$$

Taking the partial of each moment with respect to the appropriate body rate results in the three stability derivatives given below in Equation 4.

$$\begin{aligned}
C_{M_q} &= \frac{\partial C_m}{\partial q} \\
C_{N_r} &= \frac{\partial C_n}{\partial r} \\
C_{\mathcal{L}_p} &= \frac{\partial C_{\mathcal{L}}}{\partial p}
\end{aligned} \tag{4}$$

The vehicle is trimmed at an angle of attack when the pitching moment coefficient, C_m , is zero for a given freestream condition. For a fixed vehicle outer mold line, the trim angle of attack is a strong function of the CG of the vehicle. The trim angle of attack and CG strongly affect the vehicle $\frac{L}{D}$, which affects the downrange and crossrange capability.

In general, when at steady-state and with no body rates, the Orion trim angle of attack is primarily a function of the vehicle mass properties, free-stream velocity, Mach number, and whether or not parachutes are deployed. Since the control authority of the vehicle has effectively no impact on those characteristics it also has no impact on the vehicle's trim angle of attack, excluding the velocity increase from the small translation burn performed in exoatmospheric flight. An analytical expression for trim angle of attack can be determined for the capsule without aerodynamic or control effectors.⁴

D. Orion RCS

Orion is being designed to fly a guided three-axis controlled entry trajectory. The MPCV Reaction Control System (RCS) includes twelve thrusters designed to produce sufficient values of force at steady state vacuum conditions as well as adequate values of force at steady state sea-level conditions. Of the twelve jets, four thrusters (RCS 0,1,6,7) are for roll channel control, four thrusters (RCS 2,3,8,9) are for pitch channel stability, and four thrusters (RCS 4,5,10,11) are for yaw channel control. Hence, either string A of thrusters (Jet #0→#6) or string B of thrusters (Jet #7→#11) is able to provide three-axis control to a certain level. Each channel is designed to be controlled with two thrusters and have two redundant thrusters to account for potential failures. Although, current designs include using both sets of jets as necessary to improve control performance throughout nominal trajectories.

Below in Table 1 are the thrust values at the two design flight conditions.

Flight Condition	Thrust Magnitude [lb _f]
Vacuum	160
Sea Level	110

Table 1. Table of Control System Jet Thrust for Two Design Conditions

Specifically for the Orion EFT-1 mission, in order to balance propellant usage across the two strings over the mission, the GN&C team is planning to switch the active string configuration at three points during the mission. From CM-SM separation to EI the string B will be active. From EI to drogue parachute deployment string A will be active. Finally from drogue parachute deployment to landing touchdown both string A and B will be active providing dual string control.

As this schedule could change in the future, the analysis presented in this document assumes that the most effective string (i.e. the string that provides the most torque in the relevant direction) is available and active for single-string use, and that the other, slightly less effective, string is available for dual-string use.

II. Control Authority

The potential torque that the RCS system can impart in each channel is dependent upon the placement of the thrusters relevant to the location of the vehicle center-of-gravity. The torque values in Table 2 and Table 3 were calculated by using each jet at vacuum conditions, the EI vehicle CG location, and unscarfed thrust directions. Table 2 below shows the torque produced by each jet in each axis. Table 3 below shows the approximate resulting control authority in each channel when using one thruster or two thrusters.

Jet Number	Attitude Channel	General Direction	Torque [$lb_f \cdot ft$]
1	Roll	Right	875
2	Roll	Left	-875
3	Pitch	Up	1075
4	Pitch	Down	-900
5	Yaw	Right	1025
6	Yaw	Left	-1025
7	Roll	Right	900
8	Roll	Left	-900
9	Pitch	Up	1075
10	Pitch	Down	-900
11	Yaw	Right	1025
12	Yaw	Left	-1025

Table 2. Table of Control System Torque Capability Per Jet at EI

Attitude Channel	1 String: 2 Thrusters [$lb_f \cdot ft$]	2 Strings: 4 Thrusters [$lb_f \cdot ft$]
Roll	900	1775
Pitch	1075	2150
Yaw	1025	2050

Table 3. Table of Control System Torque Capability at EI

III. Results

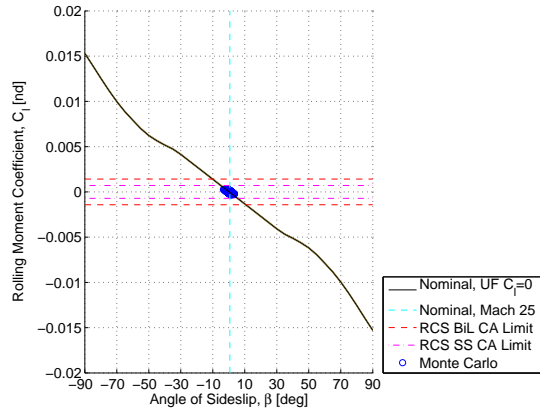
A. Static and Dynamic Stability at Various Entry Conditions

In this section several aerodynamic moment coefficients and aerodynamic moment derivative coefficients with respect to angle of attack and angle of sideslip have been provided. For comparison, the requirements for static stability in roll, pitch, and yaw are provided below in Equation 5.

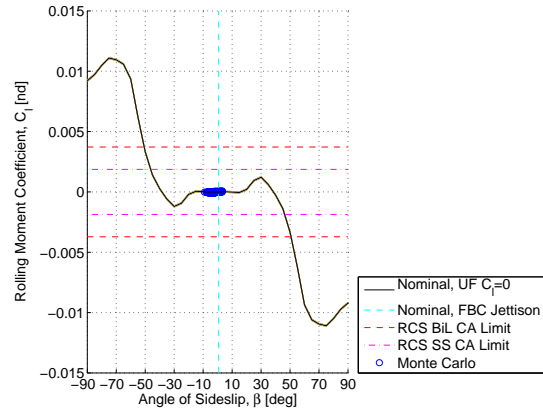
Two flight states that are of key design importance for EDL design are when Mach number equals 25 and when the Forward Bay Cover (FBC) is jettisoned. When Mach number is equal to 25 the adequacy of the hypersonic $\frac{L}{D}$ of the capsule is evaluated. If the $\frac{L}{D}$ is too small then guidance algorithm will be unable to reach the landing site for a given initial state of position and velocity. Hence it is important to know the aerodynamic characteristics of the vehicle at this state. When the FBC is jettisoned during subsonic flight the vehicle is highly sensitive to aerodynamic and atmospheric dispersions. This event is evaluated throughout design progression to ensure that the FBC jettison state supports all objectives, and changes are made so that it does support all mission objectives.

The set of plots below in Figure 4 illustrates the aerodynamic moment coefficients relationships to α , β , Monte Carlo results and RCS control authority at two key vehicle events. In Figure 4 the undispersed aerodynamic moment coefficients are illustrated, with uncertainty factor (UF) equal to zero, by black lines. Around each undispersed value the potential values with uncertainties (in the aerodynamic model) are painted in yellow. The nominal relevant angle of attack, α , or angle of sideslip, β , are indicated by a vertical cyan line. The RCS control authority in the relevant axis is indicated by a red dashed line for dual-string RCS and by a magenta dashed line for single-string RCS. In addition a Monte Carlo distribution of 3000 trajectories using only single-string RCS are plotted for the two discrete events along the trajectory. The Monte Carlo data points are colored blue if they fall inside the dual-string RCS control authority (CA), and dark red when they fall outside the dual-string RCS CA. Note that the mean, μ , of the Monte Carlo distribution does not directly correlate to the nominal undispersed trajectory. Additionally, note that the reason that some Monte Carlo points appear outside of the dispersed area painted on these figures is that the flight condition for the Monte Carlo point and the nominal point were not equivalent. For example, at FBC jettison the Monte Carlo trajectory point does not necessarily have the same free stream velocity, angle of attack, angle of sideslip or body attitude rates. Hence, as the yellow area was constructed using the uncertainties around only the nominal undisposed trajectory flight condition, the Monte Carlo points provide a measure of comparison but not a completely equivalent one. Furthermore, the RCS torque plotted is the available torque to correct the indicated aerodynamic moment. For example, in the C_m versus α plot below in Figure 4(c) the RCS torque capability that could work to correct a negative pitching moment, $-C_m$ (negative rotation about the y-axis), was plotted on the negative side of the C_m axis. Hence that RCS torque value would actually be in the $+T_y$ direction (positive rotation about y-axis direction). This method of plotting the available control authority on the same side of the vertical axis as the aerodynamic moment was done for ease in comparison, but realize that the actual RCS torque capabilities are the opposite sign as the y-axis indicates.

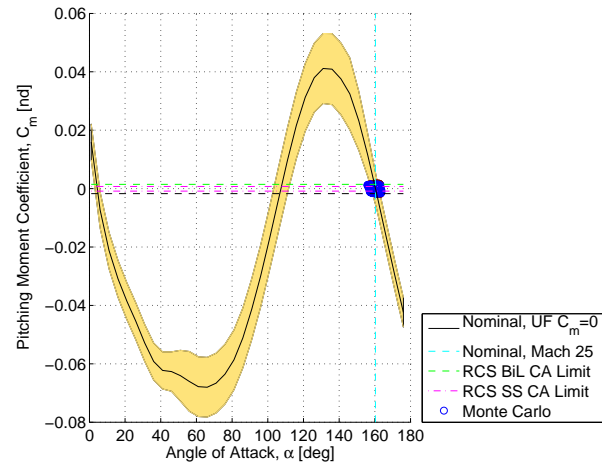
Figures 4(a) and 4(b) demonstrate how the uncertainty in the rolling moment coefficient is decreased substantially from the other two moment coefficients, due to the vehicle's symmetry about the x-axis.



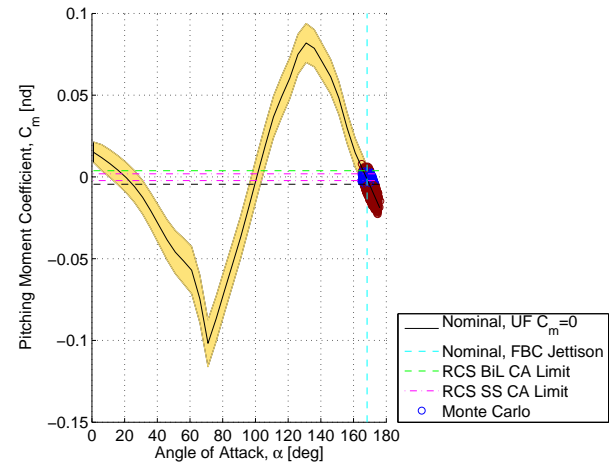
(a) Mach 25



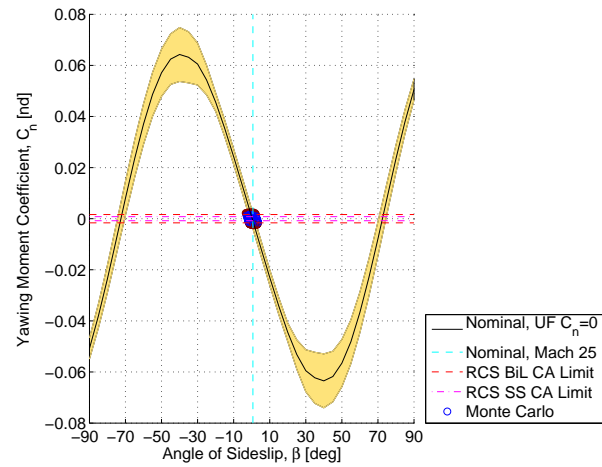
(b) FBC Jettison



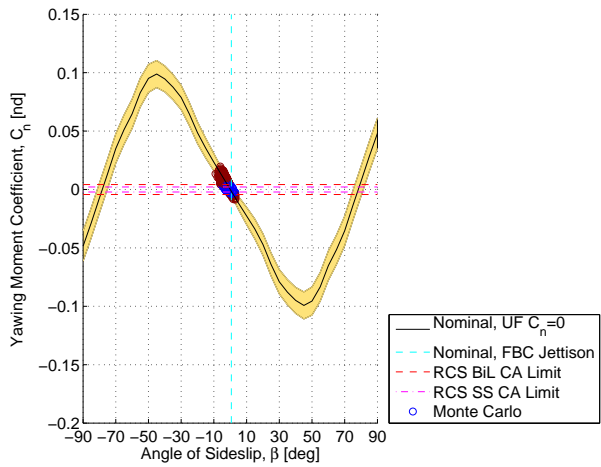
(c) Mach 25



(d) FBC Jettison



(e) Mach 25



(f) FBC Jettison

Figure 4. Aerodynamic Moment Coefficients

Table 4 below shows several aerodynamic moment coefficients for the nominal undispersed case. For comparison, the classic requirements for static stability in pitch, yaw and roll are provided below in Equation 5.

$$\begin{aligned} \text{Roll} &: C_{\mathcal{L}_\beta} < 0 \\ \text{Pitch} &: C_{m_\alpha} < 0 \\ \text{Yaw} &: C_{n_\beta} > 0 \end{aligned} \quad (5)$$

Note, that due to Orion flying backwards, with angle of attack defined relative to a vector out the apex of the vehicle rather than out the heat shield, the yaw stability convention for Orion different from Equation 5. This convention is provided below in Equation 6.

$$\text{Yaw} : C_{n_\beta} < 0 \quad (6)$$

Aerodynamic Coefficient	Event: Mach 25	Event: FBC Jettison
$C_{\mathcal{L}}$	-5.27066e-05	1.3603e-06
C_m	1.21695e-04	-0.00145
C_n	-9.26300e-04	-0.00152
$C_{\mathcal{L}_\beta}$	-1.36362e-04	-1.26175e-06
C_{m_α}	-0.00270	-0.00226
C_{n_β}	-0.00236	-0.00227

Table 4. Aerodynamic Coefficients at Specific Flight Events

From Table 4 above it is clear that at Mach number 25, and at FBC Jettison, the vehicle is statically stable in roll, pitch and yaw. As an example, Figure 5(a) and 5(b), rescoped versions of 4(e) and 4(f), are provided below with the cases that are outside the vehicle's control authority shown in dark red.

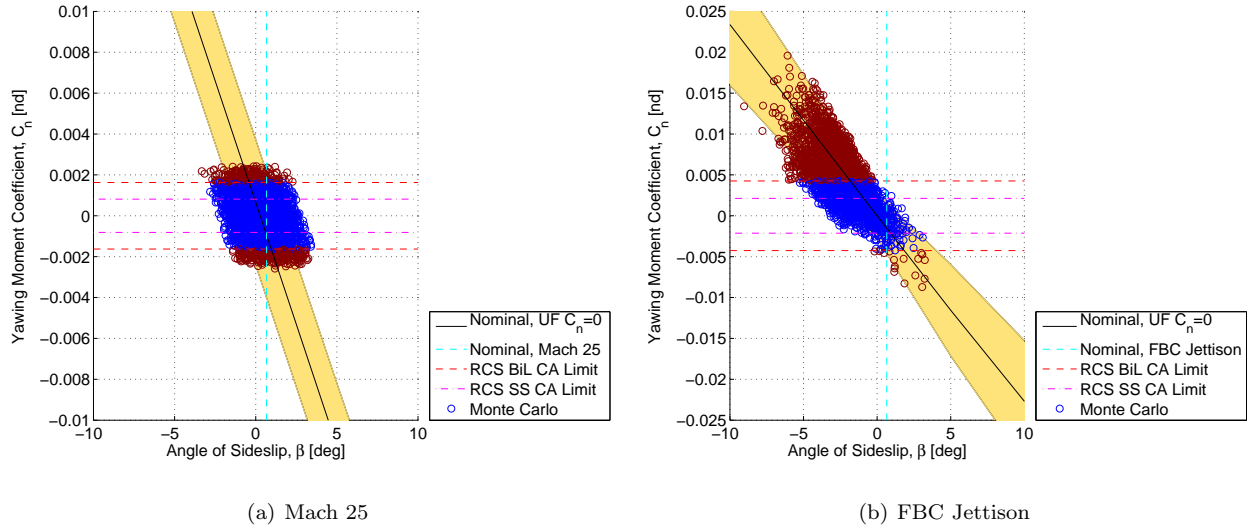


Figure 5. Aerodynamic Yawing Moment Coefficients

B. Effect of Stability Derivatives on Performance Metrics

At subsonic Mach numbers the vehicle's stability is highly sensitive to the uncertainty factors on the aerodynamic stability derivatives C_{m_q} and C_{n_r} . The plots, in Figure 6, show the variation of the aerodynamic stability derivatives uncertainty factors with angle of attack and angle of sideslip.

Table 5 below shows two important aerodynamic damping derivative coefficients for the nominal undispersed case.

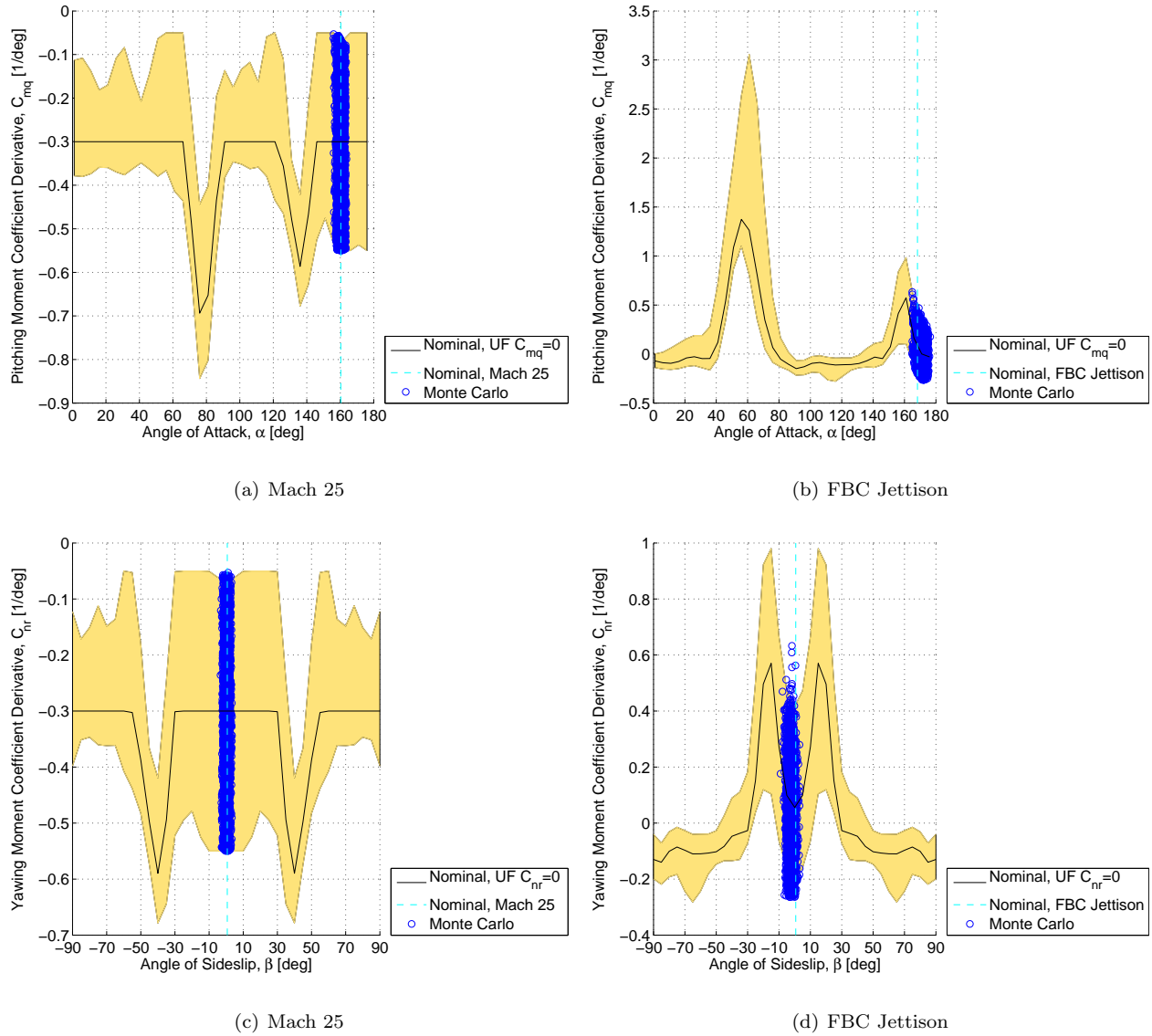


Figure 6. Moment Coefficient Derivative

The vehicle is dynamically stable when the dynamic stability derivatives C_{mq} and C_{nr} are positive. Hence, Figure 6 demonstrates that at hypersonic speed, Mach number equals 25, the vehicle is dynamically stable. Whereas Figure 6 demonstrates that at subsonic speed, at FBC jettison, the vehicle is dynamically unstable.

The reason the dynamic stability at hypersonic flight is that during hypersonic flight the dynamic pressure is larger and the positive pitch stiffness of the vehicle subsequently nulls out any small divergence caused by C_{mq} . Whereas in subsonic flight, the dynamic pressure is too small to yield a sufficient aerodynamic restoring moment. See Figure 6 for an illustration of the spike in C_{mq} around particular values of α at subsonic flight conditions.

As these two aerodynamic stability derivatives increase the vehicle becomes more unstable to perturbations caused by dispersions during free flight. As the trajectory design process includes risk evaluation as a component of measurement, if the number of successes does not meet a defined metric then the increase risk of failure must be accepted or the entry trajectory must be redesigned. This instability presents a challenge to EDL events such as parachute deployments. For example in the case of subsonic atmospheric re-entry flight where the aerodynamic stability derivatives are significant, a common metric is the number of cases that are allowed to fail by diverging from heat shield forward toward apex forward (via a certain α limit) at

Aerodynamic Coefficient	Event: Mach 25	Event: FBC Jettison
C_m	1.21695e-04	-0.00145
C_n	-9.26300e-04	-0.00152
C_{m_q}	-0.3	0.76780e-03
C_{n_r}	-0.3	0.09870

Table 5. Aerodynamic Coefficients at Specific Flight Events

some point during re-entry. This type of divergence typically occurs due to aerodynamic instability and a lack of control authority to null the produced vehicle rates. This metric was significant in the design selection of the planned FBC jettison condition and drogue chute deployment condition. The vehicle must be able to complete those two events while oriented nominally in the flow with the heat shield forward with respect to the velocity direction.

C. Control Authority Impacts on GN&C

D. Aerodynamic RCS Jet Interaction Control Authority Impacts on GN&C

1. Methodology

This analysis was performed as a verification of the sensitivity of the GN&C system to aerodynamic RCS jet interaction via an alteration of the the thrust direction alone. This analysis assumed that the nozzle scarf effects and the RCS jet interaction effects on the thrust magnitudes were zero.

To provide a rough sensitivity to aerodynamic jet interaction effects on the four RCS roll thruster directions, the thrust vectors were parametrically swept through planar rotations from the initial orientations to the maximum torque possible orientations in the pitch plane. Hence, by simulating a value of potential vector redirection, the sensitivity of the GNC system to pitch disturbances caused by a redirected roll thruster was modeled.

The thrust vectors of the roll jets were redirected using a planar rotation about the y-axis as illustrated in Figure 7. Note this rotation rotates the torque produced by the roll jets from a roll torque to a pitch torque.

$$F'_{jet0,1,6,7} = R_\theta F_{jet0,1,6,7} \quad (7)$$

where

$$R_\theta = \begin{bmatrix} \cos\theta & 0 & \sin\theta \\ 0 & 1 & 0 \\ -\sin\theta & 0 & \cos\theta \end{bmatrix} \quad (8)$$

The torque created on the vehicle by each jet is given by Equation 9 below.

$$T = \widetilde{r_{jet}} F \quad (9)$$

where

$$\begin{aligned} T &= \text{Torque} \\ r_{jet} &= \text{Position vector from CG to jet} \\ F &= \text{Thrust force of jet} \end{aligned}$$

Hence, using the position vector skew symmetric matrix translates to Equation 10 below.

$$T = \begin{bmatrix} 0 & -r_z & r_y \\ r_z & 0 & -r_x \\ -r_y & r_x & 0 \end{bmatrix} \cdot \begin{bmatrix} F_x \\ F_y \\ F_z \end{bmatrix} \quad (10)$$

$$T_y = r_z \cdot F_x - r_x \cdot F_z \quad (11)$$

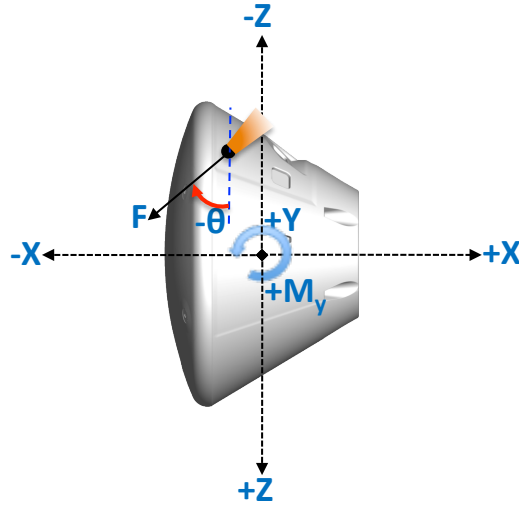


Figure 7. Orientation of planar rotation R_θ about $+Y^{[GNCBody]}$

To complement the thrust direction sensitivity a thrust magnitude sensitivity was performed. The thrust magnitudes of the roll jets were scaled from 100 percent to 60 percent of nominal thrust. As a result of this thrust reduction the control authority in the roll channel, and also the yaw channel due to the coupled thrust direction, was decreased.

2. Results

The RCS data presented below in Figure 8 is for statistics from Entry Interface (EI) to drogue chute deployment. Drogue chute deployment happens a only small number of seconds after FBC Jettison. Note, that the drogue chute deployment state and FBC jettison state are close in time and linked so that at least for the data metrics presented below, the two states are closely comparable.

The sensitivity of three RCS control system metrics are shown below in Figure 8 as a function of thrust rotation angle, θ . These three metrics are propellant usage, number of jet pulses, and cumulative on-time for each channel of jets

As the rotation is increased the effectiveness of the roll jets in the roll channel is reduced and the perturbation produced in the pitch channel is increased. The effect of this is generally an increase in the propellant usage, pulse count and cumulative on-time for each channel. The sensitivity increases incrementally until at a rotation angle of 90° which completely rotates the roll jet into a pitch thrusting jet. As the expectation is that a aerodynamic jet interaction would be unlikely to surpass $\pm 20^\circ$, this analysis provided input to support the notion that the vehicle design did not need to be changed due to the effect of aerodynamic jet interaction.

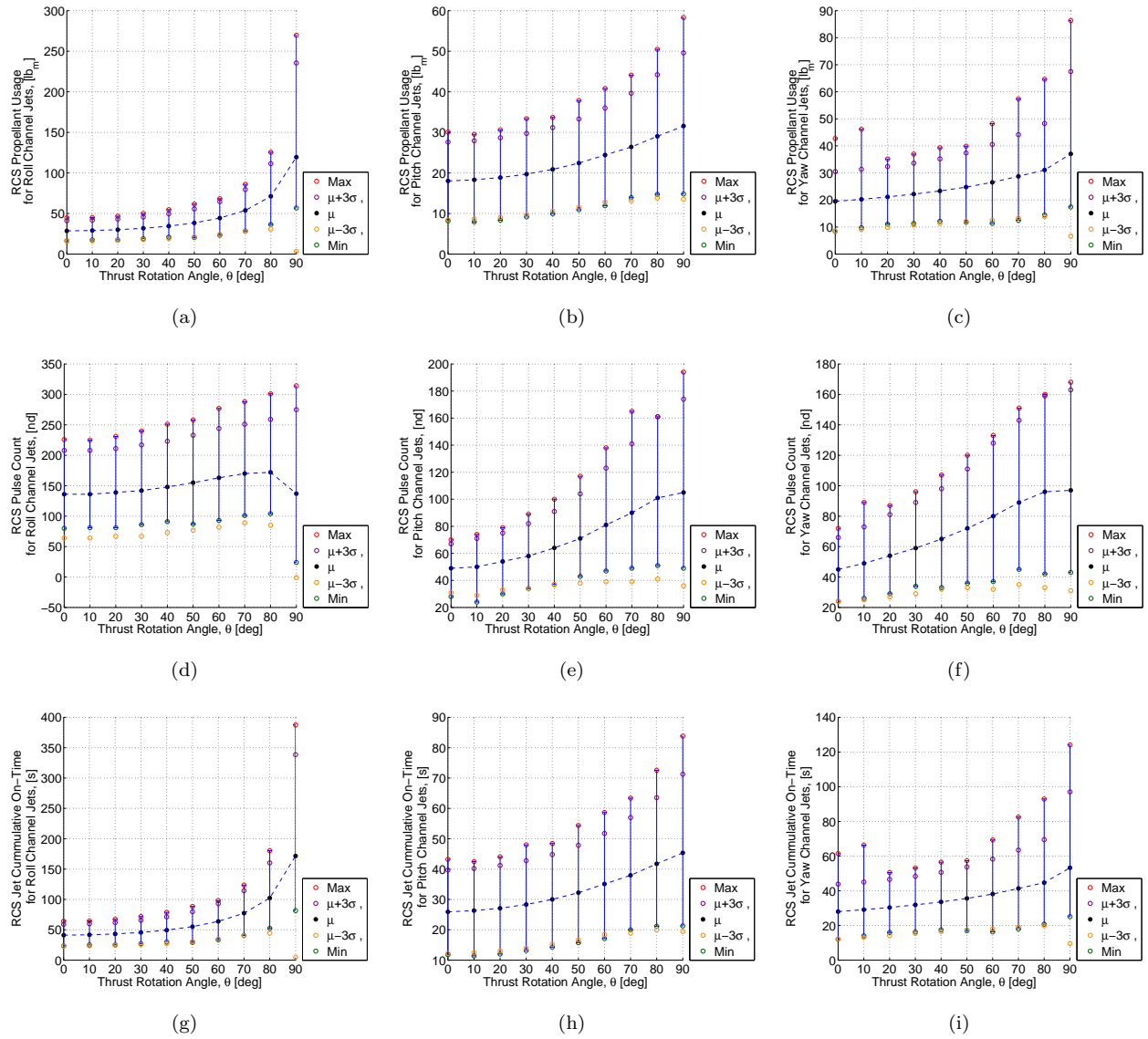


Figure 8. RCS Performance for Various Artificial Thrust Vector Rotations to Simulate Aerodynamic RCS Jet Interaction

The sensitivity of three integrated EDL key performance metrics are shown below in Figures 9, 10, and 11 as a function of thrust rotation angle, θ . These three metrics are bank angle saturation, aerothermal $Re_{\theta'}$, and landing target accuracy.

The bank angle is the only mechanism during atmospheric flight that the PredGuid entry guidance algorithm uses to target the landing site. In order to orient to, and hold at, a desired bank angle the RCS roll and yaw jets are pulsed as necessary to generate sufficient roll and yaw acceleration.

The bank angle is defined to be 0° when oriented purely lift-up and 180° when oriented purely lift-down. When the vehicle is flying with the bank angle oriented lift up ($0^\circ \pm 15^\circ$) or lift down ($180^\circ \pm 15^\circ$) the bank angle is saturated. If the vehicle is saturated lift-up or lift down, it is typically because the desired target is outside the longitudinal capabilities of the vehicle given the initial condition state vector, vehicle L/D capability, atmospheric properties and model dispersions.

The bank saturation metric defined below in Equation 12 describes the fraction of time, during the Apollo Final Phase portion of the PredGuid algorithm, that the vehicle is bank saturated. The bank saturation metric is defined from zero to one.

$$\text{Bank Saturation} = \frac{T_{SAT,F} - T_{SAT,O}}{T_F - T_O} \quad (12)$$

where

$T_{SAT,F}$	=	Time spent saturated at end of Final Phase Guidance
$T_{SAT,O}$	=	Time spend saturated at beginning of Final Phase Guidance
T_F	=	Elapsed time at end of Final Phase Guidance
T_O	=	Elapsed time at beginning of Final Phase Guidance

The EDL trajectory is designed to keep bank angle saturation below a percentage level (50%) to enable the vehicle to reach its target landing site in the presence of dispersions. Figure 9 below illustrates the sensitivity of increasing the thrust rotation angle on the bank angle saturation metric. From this figure it is clear that the distribution mean, μ , and $\mu + 3\sigma$ are relatively insensitive until θ equals 90° , and the maximum is relatively insensitive until θ equals 70° . Note that σ is defined as the standard deviation of the distribution.

Figure 10 illustrates the sensitivity of the aerothermal parameter $Re_{\theta'}$ which was defined in Equation 1 at a point on the Leaside Dish of the vehicle. It is a flight test objective to achieve a value greater than 250 for a freestream velocity greater than $20,000 \frac{ft}{sec}$. Note, on the plot the lower hatched area indicates a minimum design constraint to stay above in order to meet this objective. From θ equals 0° to 90° the maximum $Re_{\theta'}$ is relatively insensitive which would make intuitive sense if the vehicle $Re_{\theta'}$ were not a function of the RCS system plume impingement heating. The impact of RCS system plume impingement heating is being assessed during the design process.

The two plots in Figure 11 below illustrate the impact of rotation angle on the vehicle target accuracy probability at the drogue deployment state. The drogue deployment state typically offers a good assessment of the final landing condition ignoring the impacts of winds and parachute drift. It is a flight test objective to land within 10.8 nautical miles of the landing target. The hatched area of the plots in Figure 11 below indicate this design constraint. From this figure it is clear that the distribution mean, μ , is relatively insensitive to θ and the maximum is relatively insensitive until θ equals 60° .

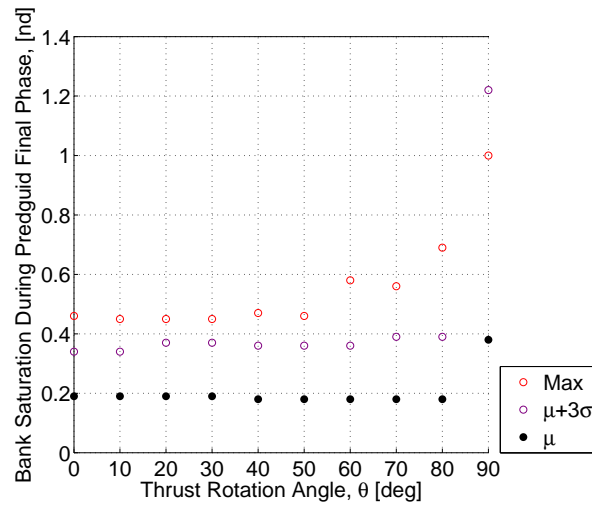


Figure 9. Bank Saturation Performance Metric for Various Roll Jet Thrust Vector Rotations

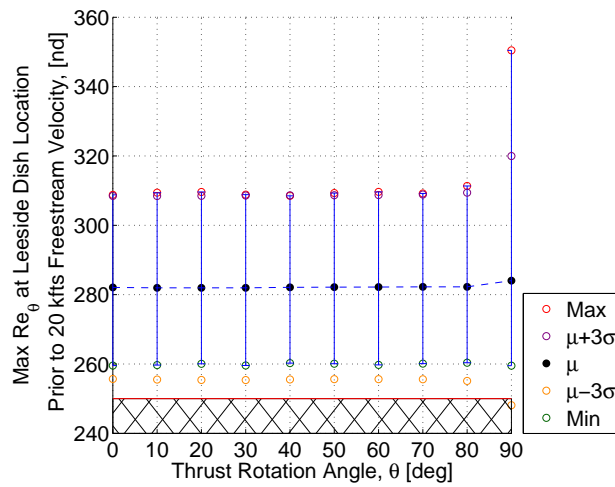
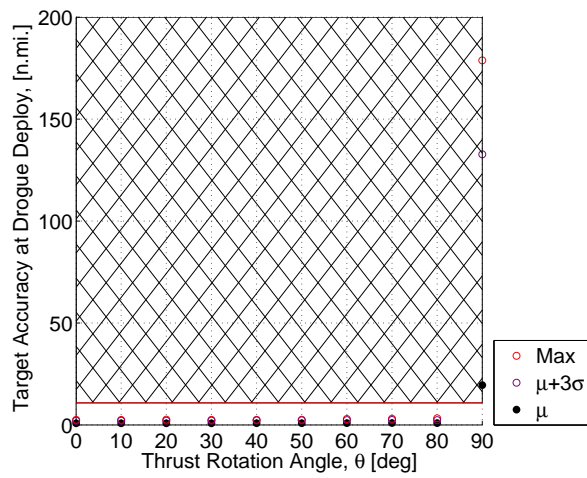
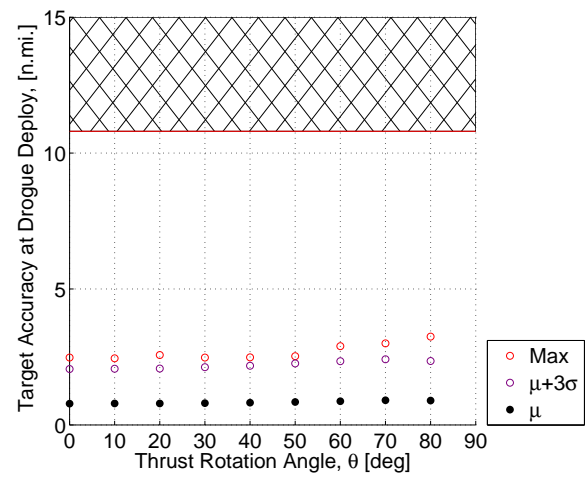


Figure 10. Re_θ Performance Metric for Various Roll Jet Thrust Vector Rotations



(a) Full Scope



(b) Focused Scope

Figure 11. Target Accuracy for Various Roll Jet Thrust Vector Rotations

The sensitivity to a decrease in the roll jets thrust due to aerodynamic interactions is captured in Figure 12, 13, and 14.

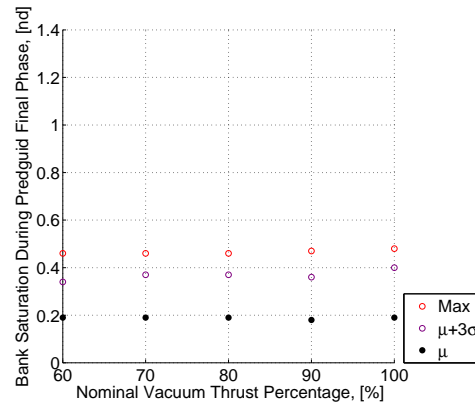


Figure 12. Bank Saturation Performance Metric for Various Roll Jet Thrust Magnitudes

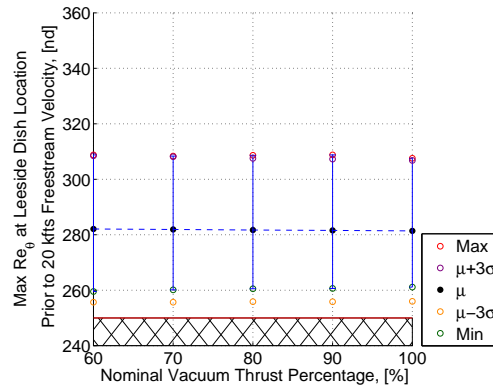


Figure 13. Re_θ Performance Metric for Various Roll Jet Thrust Magnitudes

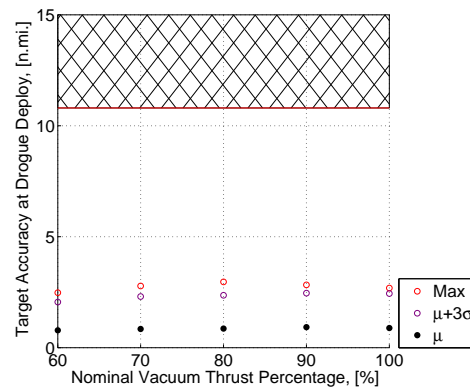


Figure 14. Target Accuracy for Various Roll Jet Thrust Magnitudes

The decrease in thrust magnitude during this phase of flight has statistically low impacts on all three of the metrics in Figure 12, 13, and 14 with the most sensitive metric being bank saturation. This is not unexpected as the full thrust of the jets is needed most after drogue chute deployment to arrest vehicle rates and to satisfy other requirements.

IV. Conclusion

For the EFT-1 trajectory simulated, at Mach number 25, and at FBC Jettison, the vehicle is statically stable in roll, pitch and yaw. The aerodynamic stability and control authority of the Orion vehicle should be monitored throughout the design process. This work will be utilized for the GN&C evaluation of future MPCV aerodynamic database releases.

Orion's performance against several of its key EFT-1 flight dynamics requirements is relatively insensitive to small degradations in the control system's ability to track bank angle, and to damp perturbations in the pitch channel and roll channel. The data presented here demonstrates that Orion can perform adequately, albeit less efficiently in terms of propellant usage, if the effective thrust direction of the RCS roll jets is up to $\pm 20^\circ$ from the design vector directions with minimal effects on integrated trajectory performance. The data also shows the vehicle can handle the thrust magnitudes up to 40% less than the design thrust level of the RCS roll jets with respect to flight objectives prior to drogue chute deployment. These indicate the robustness of the system to the worst expected aerodynamic RCS jet interaction.

The control authority assessment presented here shows that the Orion vehicle has sufficient control to handle flight dynamics for key events at most dispersion levels to accomplish EFT-1 test objectives. This work has been presented to Orion designers and has led to discussions about re-evaluating the aerodynamic RCS plume jet interaction analysis done to date.

Acknowledgments

This work was carried out by the NASA Johnson Space Center. The author would like to thank Brian R. Hoelscher, Jeremy R. Rea, and Chris M. Madsen of NASA Johnson Space Center for discussions that aided this work.

References

- ¹McNamara, Luke W., "Orion Flight Test 1 Periodic Technical Review 3 Six Degree-of-Freedom Aerodynamic RCS Jet Interaction Sensitivity Analysis," Tech. Rep. FltDyn-CEV-12-32, NASA Johnson Space Center, Houston, TX, December 2011.
- ²McNamara, Luke W., "Orion Flight Test 1 Periodic Technical Review 2 Entry Trajectory GNC Specification Evaluation," Tech. Rep. FltDyn-CEV-11-80, NASA Johnson Space Center, Houston, TX, September 2011.
- ³McNamara, Luke W., "Orion Flight Test 1 Periodic Technical Review 3 Six Degree-of-Freedom Entry Trajectories With RAMSES Flight Software Version 6.1," Tech. Rep. FltDyn-CEV-11-128, NASA Johnson Space Center, Houston, TX, October 2011.
- ⁴Rea, Jeremy R., "Orion Entry Performance-Based Center-of-Gravity Box," AIAA Guidance, Navigation and Control Conference and Exhibit, No. 2010-8061 in AIAA, August 2010.
- ⁵Carnahan, Jeremy, "OFT-1 Reference Trajectory Targets," CEV-MA-11-009, Orion Mission Analysis, Lockheed Martin Space Systems Co., Denver, CO, August 8, 2011.
- ⁶Morth, R., Reentry Guidance for Apollo, MIT/IL R-532 Vol. I, 1966.
- ⁷Putnam, Zachary R., Neave M. D., Barton G. H., "PredGuid Entry Guidance for Orion Return from Low Earth Orbit," IEEE Aerospace Conference, No. 05447010, 2010.
- ⁸Lockheed Martin Space Systems Co., "CEV-T-078: Guidance Navigation and Control Data Book, Vol. 6-7," , Denver, CO, May 2012.
- ⁹Briles, Amanda, "ANTARES V11.1.0 Release," CEV Flight Dynamics Team, NASA Johnson Space Center, Houston, TX, January, 2011.
- ¹⁰Lockheed Martin Space Systems Co., "PTR3 Orion Flight Test-1 Simulation Data Book for Project Orion," LM-ORN-0434, Revision 002, Denver, CO, August 3, 2011.
- ¹¹MPCV Aerodynamics Team, "Orion Aerodynamic Databook, Ver 0.60," NASA CXP-72167, NASA Johnson Space Center, Houston, TX, January 2011.
- ¹²NASA, "Orion MPCV," <http://www.nasa.gov/exploration/systems/mpcv/>, last accessed 14 June 2012.